Caught in the Act: Anthrax Toxin Translocation Complex Reveals insight into the Lethal Factor Unfolding and Refolding mechanism

Alexandra J Machen[1], Mark T Fisher*[1], Bret D Freudenthal*[1]

[1]Department of Biochemistry and Molecular Biology, University of Kansas Medical Center, Kansas City, KS 66160, USA.

*Co-corresponding Authors. Correspondence to bfreudenthal@kumc.edu

ABSTRACT

Translocation is essential to the anthrax toxin mechanism. Protective antigen, the translocon component of this AB toxin, forms an oligomeric pore with three key clamp sites that aid in the efficient entry of lethal factor or edema factor, the enzymatic components of the toxin, into the cell. LF and EF translocate through the protective antigen pore with the pH gradient between the endosome and the cytosol acting as the driving force. Structural details of the translocation process have remained elusive despite their biological importance. To overcome the technical challenges of studying translocation intermediates, we developed a novel method to immobilize, transition, and stabilize anthrax toxin. Here, we report a cryoEM snapshot of PA_{pore} translocating the N-terminal domain of LF. The resulting 3.1 and 3.2 Å structures of the complex trace LF_N as it unfolds near the α clamp, translocates through the Φ clamp, and begins to refold in the charge clamp. In addition, helical density inside the β barrel channel suggests LF secondary structural elements begin to refold at the charge clamp site. We conclude the anthrax toxin uses an extended β barrel to efficiently fold the enzymatic payload prior to channel exit. This refolding mechanism has broader implications for pore length of other protein translocating toxins.

16 **INTRODUCTION**

17 The anthrax toxin is not only a deadly *Bacillus anthracis* virulence factor, but also serves
18 as a model system of protein translocation and as a peptide therapeutic delivery platform (Young
19 and Collier 2007, Thoren and Krantz 2011). It's biological importance and biotechnology utility
20 have spurred significant biochemical and biophysical advances in understanding the anthrax
21 intoxication mechanism. In order to gain entry into the cell, this archetypical AB toxin must cross
22 the endosomal membrane. This is accomplished by the B component of anthrax toxin, termed
23 protective antigen (PA). PA forms a translocon pore through which lethal factor (LF) or edema
24 factor (EF), the A component, translocate. Here, we developed an approach to elucidate the
25 structural and mechanistic details of the anthrax toxin during translocation in an effort to
26 understand how LF unfolds in the endosome, translocates through PA, and refolds in the cytosol.

27 An overview of the anthrax toxin mechanism has been reviewed by the Collier lab (Young
28 and Collier 2007) and is briefly summarized here. The first step in intoxication is the 85 kDa
29 monomeric PA binding to host cell receptors. Then the pro-domain of PA is cleaved leaving the
30 63 kDa PA to oligomerize into heptameric or octameric prepore ($PA_{prepore}$) (Santelli, Bankston et
31 al. 2004, Kintzer, Thoren et al. 2009). Up to three LF and/or EF components can bind to the
32 $PA_{prepore}$ heptamer (Mogridge, Cunningham et al. 2002, Kintzer, Thoren et al. 2009, Antoni,
33 Quentin et al. 2020). The AB toxin complex is endocytosed through clatherin mediated
34 endocytosis (Abrami, Liu et al. 2003). As the endosome acidifies, $PA_{prepore}$ undergoes a
35 conformational change to a pore (PA_{pore}) (Miller, Elliott et al. 1999). This pore inserts into the
36 endosomal membrane to form a channel and create a pH gradient. With the pH gradient as the
37 driving force, LF or EF unfold and translocate into the cytosol using a hypothesized Brownian

38 ratchet mechanism (Krantz, Finkelstein et al. 2006). Natively refolded LF and EF in the cytosol
39 are then able to perform their virulent enzymatic functions (Duesbery, Webb et al. 1998).

40 The overall structure of the PA_{pore} translocon can be divided into two regions: the funnel
41 and the channel (**Figure 1A**). The first region, the funnel, facilitates binding and unfolding of LF.
42 LF binds to the rim of the PA_{pore} funnel and is guided down the narrowing structure. The second
43 region of PA_{pore} is the channel, a β barrel that extends from the funnel and spans the endosomal
44 membrane. Three nonspecific PA_{pore} clamp sites aid in the translocation of LF (**Figure 1A**). The
45 α clamp is located at the PA funnel rim, is formed by adjacent PA protomers, and binds helical
46 portions of LF to position them towards the pore lumen. A crystal structure of the N-terminal
47 domain of LF (LF_N) bound to the $PA_{prepore}$ revealed the α clamp binding site, but was unable to
48 resolve the 28 amino acids of LF_N passed the α clamp (Feld, Thoren et al. 2010). The second clamp
49 site is the Φ clamp, a ring of seven phenylalanine residues that maintain the pH gradient between
50 the endosome and the cytosol (Krantz, Melnyk et al. 2005). The 2.9 Å structure of apo PA_{pore}
51 revealed the Φ clamp forms a narrow 6 Å diameter ring (Jiang, Pentelute et al. 2015). Secondary
52 structural elements, such as α helices, are too wide to fit through this narrow seal. Therefore, it is
53 hypothesized that peptide substrates must completely unfold and refold in order to translocate
54 through the PA_{pore} and enter the cytosol of the cell (Jiang, Pentelute et al. 2015). The Φ clamp also
55 assists in the unfolding of LF as an unfolding chaperone (Thoren and Krantz 2011). The third
56 clamp site, the charge clamp, is located within the β barrel of PA_{pore}. The charge clamp
57 deprotonates acidic side chains of LF and ensures unidirectional movement of the polypeptide
58 (Pentelute, Sharma et al. 2011, Brown, Thoren et al. 2015). Interestingly, the diameter of the PA_{pore}
59 β barrel is large enough to accomidate an α helix, which would allow for initial refolding to occur

60 inside the pore prior to LF entering the cytosol. However, it remains unclear what structural state
61 LF is in when interacting with the charge clamp and within the β barrel channel.

62 One of the many challenges in studying the anthrax toxin is that it is a dynamic membrane
63 protein that functions under acidic conditions. Thus many questions remain, such as what path LF
64 travels down the endosomal pore lumen from the α clamp to the Φ clamp, whether the Φ clamp
65 adopts multiple states during translocation, and whether LF forms α helices inside the β barrel
66 pore. To address these questions, we developed a novel toxin immobilization, translocation, and
67 nanodisc stabilization (TITaNS) method in combination with cryoEM to capture PA_{pore}
68 translocating the N-terminal domain of LF (LF_N). This approach provides unique mechanistic
69 insight into how LF_N translocates through the PA_{pore} by visualizing translocating LF_N interacting
70 with the three clamp sites of PA_{pore}. We observed LF_N unfolding prior to the α clamp, translocating
71 through the dynamic Φ clamp, and beginning to refold in the charge clamp of the PA_{pore}.

72

73 **RESULTS**

74 *Assembly of Anthrax Translocation Complexes*

75 The anthrax toxin requires a pH gradient or electrostatic potential for translocation with the
76 difference in pH affecting the rate of translocation (Collier 2009). Previous approaches have
77 generally used urea to transition from $PA_{prepore}$ to PA_{pore} to avoid aggregation (Katayama, Wang
78 et al. 2010, Akkaladevi, Hinton-Chollet et al. 2013, Gogol, Akkaladevi et al. 2013, Akkaladevi,
79 Mukherjee et al. 2015, Machen, Akkaladevi et al. 2017, Hardenbrook, Liu et al. 2020). These
80 approaches have limitations in that they do not account for the low pH electrostatic
81 microenvironment in the pore lumen and they assume similar outcomes for chaotrope and acid
82 induced unfolding. In order to overcome these limitations we have developed a novel assembly

83 method for toxin immobilization, translocation, and nanodisc stabilization (called TITaNS, **Figure**
84 **1B-G**). This approach allows for endosomal pH pore formation, translocation induction, and
85 imaging of individual complexes in a lipid bilayer in the biologically relevant low pH environment
86 (Machen, Akkaladevi et al. 2017, Fisher and Naik 2019). TITaNS can be used in combination with
87 techniques other than cryoEM, including mass spectrometry, nuclear magnetic resonance, surface
88 plasmon resonance, and biolayer interferometry. TITaNS can also be adapted to screen potential
89 pharmaceuticals that arrest translocons or prevent endosomal membrane insertion (Fisher and Naik
90 2019).

91 Reversible immobilization is key to the TITaNS methodology, because it allows the
92 stabilized complexes to be released from the beads. We began with recombinantly purified, soluble
93 forms of LF_N and $PA_{prepore.}$ The toxin components were incubated in solution. The binary complex
94 of LF_N bound to $PA_{prepore}$ was then immobilized onto thiol sepharose beads by covalently coupling
95 E126C LF_N to the bead surface (**Figure 1B**). The LF_N-$PA_{prepore}$ complex was immobilized on the
96 beads and oriented such that when the bead slurry was washed in pH 5.5 buffer to transition PA
97 from prepore to pore, the pore extended away from the bead surface (**Figure 1C**). To initiate
98 translocation of LF_N through PA_{pore}, the bead slurry was then washed in pH 7.5 buffer (**Figure**
99 **1D**). This creates a pH gradient that faciliates translocation of LF_N. Importantly, the covalent
100 coupling of LF_N to the beads stalled translocation prior to completion while keeping the binary
101 LF_N-PA_{pore} complex intact. These binary LF_N-PA_{pore} complexes were previously confirmed using
102 biolayer interferometry coupled with mass spectrometry and negative stain electron microscopy
103 (Machen, O'Neil et al. 2018). The next step in TITaNS was solublization of LF_N-PA_{pore}
104 translocation complexes using nanodisc technology (Denisov, Grinkova et al. 2004, Ritchie,
105 Grinkova et al. 2009, Bayburt and Sligar 2010). Pre-nanodisc micelles were added to the bead

106 slurry and associated with the transmembrane portion of PA_{pore} (**Figure 1E**). To promote lipid
107 bilayer formation we dialyzed away excess detergent (**Figure 1F**). The soluble LF_N-PA_{pore}-
108 nanodisc complexes were then eluted off the thiol sepharose beads using a reducing agent. Eluted
109 complexes at pH 7.5 were added to the cryoEM grid. Then the pH of solution on the grid was
110 dropped to pH 5.5 to capture the native complex at low pH prior to blotting and plunge freezing
111 (**Figure 1G**). Acidification of complexes was time sensitive as unfolded, partially translocated
112 LF_N would rapidly aggregate in solution at low pH and nanodiscs tended to migrate to the air-
113 water interface given enough time (data not shown). Therefore, we waited to acidify complexes
114 until they were on the cryoEM grid and plunge freeze grids within 30 seconds of sample
115 application.

116 Using our TITaNS methodology, we were able to reconstruct a 3.1 Å and a 3.2 Å cryoEM
117 map of LF_N translocating through PA_{pore} (**Figure 2A)**. We traced density of unfolded LF_N peptide
118 in the PA_{pore} translocon using local refinement, volume subtraction, and 3D variability analysis.
119 These densities were most notable near the three clamp sites within $PA_{pore,}$ suggesting the α, Φ,
120 and charge clamps stabilize translocation intermediates. Using the well-defined cryoEM densities
121 inside the pore, molecular models of LF_N translocating through the PA_{pore} were built (**Figure 2B**).
122

123 *Unfolding intermediates of LF_N during translocation*

124 Prior to translocation, LF_N is bound to the cap of PA at the interface of two PA protomers
125 with helix **α**1 bound to the α clamp (Feld, Thoren et al. 2010, Hardenbrook, Liu et al. 2020). In
126 our translocation complex, we observe density for LF_N at the interface of the two PA protomers
127 and at the α clamp. In order to explore the heterogeneity of LF_N bound to the PA cap, we used
128 symmetry expansion in combination with 3D variability analysis. The resulting vectors revealed a

129 second unfolded LF_N intermediate bound to the rim of PA_{pore} (Supplemental **Figure 1**). The
130 trajectory of these densities suggests steps in LF_N unfolding during translocation. Prior to
131 translocation, the density for LF_N is a bean shaped structure with 2 lobes (Feld, Thoren et al. 2010,
132 Machen, Akkaladevi et al. 2017). The first unfolded state shows two lobes separating. The second
133 unfolded state shows Lobe 1 translocating down the α clamp and Lobe 2 shifting counter clockwise
134 towards the α clamp, primed for translocation. Interestingly, this counterclockwise shift would
135 align full length LF, which extends from Lobe 2, directly above the α clamp for efficient unfolding
136 and translocation (**Supplemental Figure 1**). Together, these intermediates of LF_N unfolding
137 indicate LF travels through the α clamp during translocation.

138 Local refinement of the densities above the pore showed the two unfolded states of LF_N in
139 greater detail. Specifically, refined tubular densities allowed us to trace secondary structure of LF_N
140 with helical bundle and beta sheet separation compared to canonical folded LF_N (**Figure 3A**). The
141 rearrangement of LF_N suggests a translocated state with the immobilized residue E126C halting
142 further translocation (**Figure 3B-C**). Previous comparisons of folded LF_N bound to $PA_{prepore}$ vs
143 PA_{pore} noted LF_N moves up and away from the PA binding interface (Hardenbrook, Liu et al.
144 2020). Our intermediates suggest this motion trajectory continues and is important for unfolding
145 prior to translocation.

146

147 *Tracing Translocating LF_N through the clamp sites of the PA_{pore}*

148 To trace LF_N from the α clamp to the Φ clamp, we subtracted PA_{pore} model density from
149 our unsharpened map to reveal electron density in the pore lumen not accountable for the $PA_{pore.}$
150 Density started in the α clamp and traveled down the pore lumen, interacting with β sheet 39 of
151 PA_{pore}. Density near the top of the PA_{pore} cap was in proximity to several hydrophobic residues of

152 PA_{pore} (**Figure 4A**). Some of these residues, including Phe202, Phe236 and Phe464 were in the α
153 clamp and have previously been proposed to aid in unfolding LF and stabilizing unfolded
154 intermediates(Feld, Thoren et al. 2010). Additional hydrophobic residues further down the pore
155 lumen, such as Trp226, Tyr456, and Tyr375 were also near LF_N density and may help to stabilize
156 the unfolded peptide. The unfolded peptide also interacts with acidic residues Glu465, Asp426,
157 and Glu393 closer to the Φ clamp. Previously, molecular modeling using milestoning noted these
158 residues are important for early translocation events (Ma, Cardenas et al. 2017). Our results are
159 consistent with these residues facilitating translocation of LF_N into the pore in an unfolded state.

160 Added asymmetric density in and around the Φ clamp (**Figure 4C**) was seen in the final
161 refined map without further processing (e.g., local refinement, map subtraction, sharpening).
162 Compared to the previously published apo PA_{pore} cryoEM structure (Jiang, Pentelute et al. 2015),
163 the Φ clamp region in our translocating structure has added density. Specifically, density for each
164 of the Phe427 was smeared in plane with the benzyl ring suggesting rotameric states moving up
165 and down (**Figure 4D)**. There is also density in the center of the Φ clamp (**Figure 4C**). We attribute
166 this density to the unfolded LF_N interacting with PA_{pore} Φ clamp loop as LF_N is translocating
167 through the pore.

168 Density was also observed in the β barrel of the PA_{pore}. Focused refinement of the β barrel
169 interior revealed an α helical density with a portion of unfolded peptide above and below the helix
170 (**Figure 5)**. Notably, the helical density starts in the PA_{pore} charge clamp suggesting the
171 deprotonated state favors helix formation (Jas, Childs et al. 2019). Canonical charge clamp
172 residues Asp276, Glu434, and Glu335 are shown in **Figure 5** with each of the seven PA_{pore}
173 subunits contributing one residue and LF_N density translocating through the center of the channel.
174 This helical density in the charge clamp provides strong evidence for initial refolding of LF

175 secondary structure inside the PA_{pore}. The newly formed helix likley stabilizes unfolded
176 intermediates of LF as well as contributes to native folding of the enzyme upon exit of the PA_{pore}.
177

178 **DISCUSSION**

179 The anthrax toxin PA_{pore} is a nano trojan horse that unfolds, translocates, and refolds it's
180 enzymatic subtrate. Three clamp sites aid in peptide translocation: the α clamp, the Φ clamp, and
181 the charge clamp. We report here, for the first time, a trace of nascent polypeptide chain
182 translocating the length of PA_{pore}. LF_N can be seen unfolding prior to the α clamp, passing through
183 the dynamic φ clamp, and refolding in the charge clamp.

184 In order to translocate, LF must completely unfold. However, if the entire 90 kDa enzyme
185 were to unfold at once, deleterious folded intermediates or aggregates would likely block the PA_{pore}
186 translocon, especially when multiple LF are bound to PA. Therefore, in order to efficiently
187 translocate and refold, LF unfolds from the N to C terminus(Zhang, Finkelstein et al. 2004). While
188 the low pH of the endosome destabilizes the enzyme, it does not completely unfold into its primary
189 sequence (Gupta, Singh et al. 2001, Krantz, Trivedi et al. 2004). We were able to capture two
190 unfolded intermediate structures of LF_N with density for secondary strucural elements. Our results
191 suggest that molten globular translocation intermediates of LF rotate towards the α clamp. The α
192 clamp is then able to apply additional unfolding force on the protein (Thoren and Krantz 2011)
193 and funnel LF towards the Φ clamp. Translocation requires unfolding and stabilization of the
194 unfolded intermediates. When LF binds to PA_{pore}, the first helix of LF moves away from the main
195 body of LF and binds to the α clamp of PA_{pore} (Feld, Thoren et al. 2010). From here, LF has
196 multiple paths it could take through the PA_{pore} funnel, gated by the Φ clamp. Our results show a
197 favorable path from the α to Φ clamp involves a series of hydrophobic residues that are amenable

198 to unfolded translocation intermediates and likely serve as checkpoints to verify the unfolded state
199 of LF prior to the Φ clamp.

200 The Φ clamp plays a crucial roll in translocation by acting as a hydrophobic seal between
201 the endosome and cytosol (Krantz, Finkelstein et al. 2006). Multiple Φ clamp states have been
202 hypothesized at pH 5.5 (Das and Krantz 2016). While our analysis did not reveal multiple distinct
203 states, the smeared density is indicative of a dynamic clamp. The density does not imply dilation
204 of the clamp (Das and Krantz 2016), so much as a up and down motion along the pore axis. This
205 motion could be conserted or individual F427 may move to accommodate various side chains. The
206 compressive and tensile forces generated by the unfolding LF in the PA_{pore} funnel above and
207 refolding LF in the β barrel channel below may also contribute to this movement. Too much
208 flexibility or dialation would cause the seal to be lost. However, this dynamic motion maintains
209 the pH gradient between the endosome and cytosol, while accomidating any side chain, ensuring
210 efficient translocation.

211 Helix formation inside the PA_{pore} β barrel has been hypothesized but, to our knowledge,
212 never observed (Krantz, Trivedi et al. 2004, Jiang, Pentelute et al. 2015). We report here, evidence
213 of α helix formation and translocation inside the β barrel of the PA_{pore} (**Figure 5)**. Along with
214 changing the charge state of the peptide substrate, the charge clamp allows for a local folding
215 environment within the PA_{pore}. Helical portions of LF have previously been shown to dock into
216 the α clamp,with the periodicity of these helices aiding in efficient unfolding of LF (Das and Krantz
217 2017). We predict this periodicity is also important for refolding of LF, beginning in the charge
218 clamp. Our hypothesis is consistent with other anthrax toxin subtrates, such as LF_N fused to the
219 catalytic chain of diphtheria toxin (LF_N-DTA), that do not have the same helical periodicity and
220 did not evolve to fold in the PA_{pore} channel. Interestingly, these non-native substrates require

221 chaperones for enzymatic activity (Dmochewitz, Lillich et al. 2011) indicating the DTA portion
222 of these proteins do not form helices in the PA channel at optimal intervals. Thus LF_N-DTA is less
223 likely to emerge as folded intermediates therefore requiring chaperones to fold or refold properly.
224 This model is reminesant of the ribosome, where helix folding in the exit tunnel aids in co-
225 translational folding of native proteins (Wilson and Beckmann 2011). We predict helix folding in
226 the PA_{pore} β barrel aids in co-translocational folding by temporally altering LF emersion from the
227 tunnel allowing regions to fold into tertiary structures.

228 A proposed unfolding-refolding translocation model is shown in **Figure 6A** starting with
229 LF_N bound to the funnel rim of $PA_{pore.}$ LF_N lobes 1 and 2 separate and rotate counter clockwise
230 towards the α clamp as LF_N is unfolded and funnelled towards the Φ clamp, aided by hydrophobic
231 residues along the funnel slope. LF_N acidic residues are protonated in the acidic environment of
232 the funnel. Completely unfolded LF_N then passes the Φ clamp. This ring of F427 remains
233 restrictive enough to maintain a seal while cushioning the mechanical forces of translocation and
234 chemical interactions of side chains. As the channel widens in the charge clamp, acidic residues
235 are deprotonated. Folding of α helical portions would place mechanical force on the translocating
236 peptide, contributing to efficient translocation, and possibly overcoming local energy minimum
237 that would otherwise stall the complex. The newly formed, secondary structure favors
238 unidirectional translocation by discouraging retrograde transfer through the narrow Φ clamp.

239 In order to capture translocating anthrax toxin for cryoEM, we developed a novel toxin
240 immobilization, translocation and nanodisc stabilization (TITaNS) method. This method can be
241 adapted to attain intermediates of a wide range of host cell interactions under endosomal
242 conditions. Currently, the method involves immobilization on a bead based substrate with bulk
243 solution washes in an eppendorf tube which results in an ensemble of translocation complexes. To

244 obtain more descrete complexes, the method is being expanded to include immoblization on a
245 column, allowing for low pH pulse chase. E126C was selected as the immobilized residue for its
246 location with respect to the PA binding site. It also stalls the complex early in translocation.
247 Moving the immobilization residue further from the N-terminus would capture mid and late
248 translocation complexes. In the future, TITaNS could be adapted to time-lapse cryoEM which has
249 previously been used to characterize ribosome processivity (Frank 2017).

250 Aromatic gates are found in other toxin and translocation systems. PA Phe427 is equivalent
251 to Phe454 of *Clostridium perfringens* iota toxin (Knapp, Maier et al. 2015); Phe428 of *Clostridium*
252 *botulinum* C2II binary toxin (Neumeyer, Schiffler et al. 2008); and Trp318 of *Vibrio cholerae*
253 cytolysin (De and Olson 2011). It is not just bacterial toxins that use aromatic gates. Other transport
254 systems with rings of hydrophobic residues in the pore lumen include mammalian cell entry
255 (MCE) complexes (Ekiert, Bhabha et al. 2017) and proteasome-activating nucleotidase (PAN)
256 (Zhang, Hu et al. 2009). We hypothesize a dynamic hydrophobic seal model is a common
257 translocon mechanism, applicable to these other systems. TITaNS could be adapted to these
258 systems to investigate other hydrophobic seals.

259 Our results suggest the anthrax toxin has an extended β barrel channel to effeciently fold
260 its enzymatic payload. The longer pore is also necessary to interact with a receptor binding site
261 further removed from the membrane surface. Initial refolding in the pore channel is likely not
262 unique to the anthrax toxin. Indeed, other translocon shown in **Figure 6B**, such as the iota toxin
263 and TcA, have extended pores (Piper, Brillault et al. 2019). Not all pore forming toxins translocate
264 proteins. Some, like *Vibrio cholerae* cytolysin and *Staphylococcus aureus* α hemolysin, form pores
265 to distrupt ion concentrations (De and Olson 2011, Sugawara, Yamashita et al. 2015). The pore

266 length of these toxins is noticeably shorter (**Figure 6B**). We predict translocon pores have evolved
267 extended pores to faciliate substrate refolding inside the translocon for effective intoxication.
268

269 **MATERIALS and METHODS**

270 *Protein expression and purification*

271 Proteins were purified as previously described (Machen, Akkaladevi et al. 2017). Briefly,
272 His_6-SUMO-LF_N E126C was expressed in BL21 cells, purified using anion exchange, and cleaved
273 by small ubiquitin-related modifier protease (Wigelsworth, Krantz et al. 2004). Recombinant wild-
274 type PA_{83} was expressed in the periplasm of *Escherichia coli* BL21 (DE3) and purified by
275 ammonium precipitation and anion exchange chromatography (Miller, Elliott et al. 1999). After
276 trypsin activation (Wigelsworth, Krantz et al. 2004), PA_{63} heptameric prepores were formed using
277 anion exchange and size exclusion chromatography. Membrane scaffold protein 1D1 (MSP1D1)
278 was expressed from the pMSP1D1 plasmid (AddGene) with an N-terminal His-tag and was
279 purified by affinity chromatography(Ritchie, Grinkova et al. 2009).
280

281 *LF_N-PA-Nanodisc Complex formation for cryoEM with TITaNS*

282 E126C LF_N and PA were incubated in solution at a ratio of $4LF_N$:1PA. Complexes were
283 then immobilized by coupling E126C LF_N to activated thiol sepharose 4B beads (GE Healthcare
284 Bio-Sciences, Pittsburgh, PA, USA) in Assembly Buffer (50 mM Tris, 50 mM NaCl, 10mM $CaCl_2$
285 pH 7.5) at 4 °C for 12 hr. Beads were washed three times with Assembly Buffer to remove any
286 unbound PA prepores. The immobilized LF_N-PA prepore complexes were then incubated in low
287 pH buffer to transition the $PA_{prepore}$ to PA_{pore}. The beads were washed in Assembly buffer at neutral
288 pH. This wash created a brief pH gradient, with low pH near the bead surface and neutral pH in

289 the bulk solution. LF_N-PA complexes were oriented on the beads such that the cis side was near
290 the bead surface and the trans side was pointed toward the bulk solution. The dissapating gradient
291 and immobilization of LF_N to the beads stalled translocation prior to completion. After two more
292 washes with Assembly Buffer, pre-nanodisc micelles (2.5 μM MSP1D1, 97.5 μM 1-palmitoyl-2-
293 oleoyl-sn-glycero-3-phosphocholine (POPC) (Avanti, Alabaster, AL, USA), 65 (POPG) in 25 mM
294 Na-cholate (Sigma-Aldrich, St. Louis, MO, USA), 50 mM Tris, and 50 mM NaCl) were added and
295 bound to the aggregation-prone hydrophobic transmembrane β-barrel of PA_{pore}. The micelles were
296 collapsed into nanodiscs by removing Na-cholate using dialysis with Bio-Beads (BIO RAD,
297 Hercules, CA, USA). Soluble complexes were released from the thiol sepharose beads by reducing
298 the E126C LF_N-bead disulfide bond using 50 mM dithiothreitol (DTT) (Goldbio, St. Louis, MO,
299 USA) in Assembly Buffer. Assembled complexes were initially confirmed using negative-stain
300 TEM. Complexes were stored at -80C prior to cryoEM grid preparation.
301
302 *Grid preparation for cryoEM*
303 Complexes stored at -80C were thawed on ice. A glow discharged Quantifoil R1.2/1.3
304 300M Cu holey carbon grid was placed inside the FEI Vitrobot Mark IV humidity chamber at
305 100% humidity. Then, 2ul of thawed sample was applied to the grid followed by 0.5uL of 1M
306 acetate pH 5.5. The grids were then blotted and plunge frozen in liquid ethane. Frozen grids
307 were stored in liquid nitrogen prior to use.
308
309 *cryoEM data collection and image processing*
310 cryoEM grids were loaded into a FEI Titan Krios electron microscope operated at
311 300 kV for automated image acquisition with serialEM (Mastronarde 2005). cryoEM

312 micrographs were recorded as movies on a Gatan K2 Summit direct electron detection camera
313 using the electron counting mode in super resolution mode at ×130K nominal magnification, a
314 pixel size of 0.535 A per pixel, and defocus ranging between −1 and −3 µm. Total dose was
315 50.76 e-/A^2. Total exposure time was 9s and fractionated into 45 frames with 200 ms exposure
316 time for each frame. In total, 3701 micrographs were taken in a continuous session. Frames in
317 each movie were aligned and averaged for correction of beam-induced drift using MotionCor2
318 and cryoSPARC patch motion correction to generate a micrograph. Micrographs generated by
319 averaging all frames of each movie were used for defocus determination and particle picking.
320 Micrographs obtained by averaging frames 2-23 (corresponding to ~30 electrons per square
321 ångström) were used for two- and three-dimensional image classifications. The best 3,223
322 micrographs were selected for the following in-depth data processing.
323
324 *Single particle analysis and structure determination*
325 Single particle analysis was performed using cryoSPARC v2.14.2 (Punjani, Rubinstein et
326 al. 2017) (**Supplemental Figure 2**). A random subset of micrographs was selected for blob
327 particle picking. These particles were subjected to 2D classification in order to obtain a set of five
328 particle templates. Using these templates, 1,772,616 particles were selected from 3,223
329 micrographs. After multiple rounds of 2D classification, the remaining 209,513 'good' particles
330 were used to create a C7 symmetric 3D model. C7 symmetry expansion was performed on these
331 particles followed by 3D variability analysis. Three orthogonal principle modes (i.e. eigenvectors
332 of the 3D covariance) were solved with a filter resolution of 6Å. 124,919 particle from four
333 resulting clusters with potential LF_N density were selected for further processing. 3D classification,
334 consisting of two rounds of heterogenous refinements were performed. 3D classes without LF_N

335 density were discarded leaving two classes. A non-uniform refinement on the per particle motion
336 and CTF corrected particles was performed resulting in a 3.06 Å and 3.24 Å model. Resolution
337 was determined using gold standard Fourier shell correlation with a cut off of 0.143. Resolution
338 and particles distribution are shown in **Supplemental Figure 3**.

339 Local refinement was performed on the cap of the PA pore to further characterize bound
340 LF_N using a mask of LF_N (PDB 3KWV) low pass filtered to 30Å. To clearly visualize density in
341 the PA_{pore} lumen not attributable to the $PA_{pore,}$ a 3.0Å volume of PA_{pore} was created using Chimera
342 molmap (Pettersen, Goddard et al. 2004). This volume was subtracted from the cryoEM map. The
343 resulting density was sharpened in PHENIX (Adams, Afonine et al. 2010) to a resolution of 6Å
344 to obtain density of LF_N from the α to the Φ clamp. Local refinement was performed on the β
345 barrel interior using a cylindrical mask.

346

347 *Model Building and Refinement*

348 An initial model using PDB 6PSN for the PA_{pore} and PDB 3KWV for LF_N was docked
349 into the cryoEM map and corresponding LF_N local refinement map, respectively, using Chimera
350 map to model (Pettersen, Goddard et al. 2004). The PApore coarse model was then refined
351 using PHENIX real space refine (Adams, Afonine et al. 2010). Individual atomic model side
352 chains were manually adjusted to fit the density map using Coot (Emsley and Cowtan 2004).
353 This process was repeated iteratively until an optimal model was obtained. Ramachandran plots
354 and MolProbity (Chen, Arendall et al. 2010) were used to assess model quality. Supplementary
355 **Table 1** is a summary of cryoEM data collection and processing as well as model building and
356 validation.

357

ACKNOWLEDGEMENTS

This work is dedicated to the memory of our friend, mentor, and colleague Dr. Mark T. Fisher. This work was supported by National Institutes of Health (R35-GM128562 and R03-AI142361 to B.D.F.), and by University of Kansas Madison and Lila Self Graduate Fellowship to A.J.M. The authors acknowledge the use of instruments at the Electron Imaging Center for NanoMachines supported by NIH (1S10RR23057 and 1S10OD018111), NSF (DBI-1338135) and CNSI at UCLA.

365 **REFERENCES**

366 Abrami, L., S. Liu, P. Cosson, S. H. Leppla and F. G. van der Goot (2003). "Anthrax toxin triggers
367 endocytosis of its receptor via a lipid raft–mediated clathrin-dependent process." J Cell Biol **160**(3): 321-
368 328.
369 Adams, P. D., P. V. Afonine, G. Bunkóczi, V. B. Chen, I. W. Davis, N. Echols, J. J. Headd, L.-W. Hung, G. J.
370 Kapral and R. W. Grosse-Kunstleve (2010). "PHENIX: a comprehensive Python-based system for
371 macromolecular structure solution." Acta Crystallographica Section D: Biological Crystallography **66**(2):
372 213-221.
373 Akkaladevi, N., L. Hinton-Chollet, H. Katayama, J. Mitchell, L. Szerszen, S. Mukherjee, E. Gogol, B.
374 Pentelute, R. Collier and M. Fisher (2013). "Assembly of anthrax toxin pore: Lethal-factor complexes into
375 lipid nanodiscs." Protein Science **22**(4): 492-501.
376 Akkaladevi, N., S. Mukherjee, H. Katayama, B. Janowiak, D. Patel, E. P. Gogol, B. L. Pentelute, R. J. Collier
377 and M. T. Fisher (2015). "Following natures lead: on the construction of membrane-inserted toxins in
378 lipid bilayer nanodiscs." The Journal of membrane biology **248**(3): 595-607.
379 Antoni, C., D. Quentin, A. E. Lang, K. Aktories, C. Gatsogiannis and S. Raunser (2020). "Cryo-EM structure
380 of the fully-loaded asymmetric anthrax lethal toxin in its heptameric pre-pore state." bioRxiv.
381 Bayburt, T. H. and S. G. Sligar (2010). "Membrane protein assembly into Nanodiscs." FEBS letters **584**(9):
382 1721-1727.
383 Brown, M. J., K. L. Thoren and B. A. Krantz (2015). "Role of the α clamp in the protein translocation
384 mechanism of anthrax toxin." Journal of molecular biology **427**(20): 3340-3349.
385 Chen, V. B., W. B. Arendall, J. J. Headd, D. A. Keedy, R. M. Immormino, G. J. Kapral, L. W. Murray, J. S.
386 Richardson and D. C. Richardson (2010). "MolProbity: all-atom structure validation for macromolecular
387 crystallography." Acta Crystallographica Section D: Biological Crystallography **66**(1): 12-21.
388 Collier, R. J. (2009). "Membrane translocation by anthrax toxin." Molecular aspects of medicine **30**(6):
389 413-422.
390 Das, D. and B. A. Krantz (2016). "Peptide-and proton-driven allosteric clamps catalyze anthrax toxin
391 translocation across membranes." Proceedings of the National Academy of Sciences **113**(34): 9611-
392 9616.
393 Das, D. and B. A. Krantz (2017). "Secondary Structure Preferences of the Anthrax Toxin Protective
394 Antigen Translocase." Journal of molecular biology **429**(5): 753-762.
395 De, S. and R. Olson (2011). "Crystal structure of the Vibrio cholerae cytolysin heptamer reveals common
396 features among disparate pore-forming toxins." Proceedings of the National Academy of Sciences
397 **108**(18): 7385-7390.
398 Denisov, I., Y. Grinkova, A. Lazarides and S. Sligar (2004). "Directed self-assembly of monodisperse
399 phospholipid bilayer Nanodiscs with controlled size." Journal of the American Chemical Society **126**(11):
400 3477-3487.
401 Dmochewitz, L., M. Lillich, E. Kaiser, L. D. Jennings, A. E. Lang, J. Buchner, G. Fischer, K. Aktories, R. J.
402 Collier and H. Barth (2011). "Role of CypA and Hsp90 in membrane translocation mediated by anthrax
403 protective antigen." Cellular microbiology **13**(3): 359-373.
404 Duesbery, N. S., C. P. Webb, S. H. Leppla, V. M. Gordon, K. R. Klimpel, T. D. Copeland, N. G. Ahn, M. K.
405 Oskarsson, K. Fukasawa and K. D. Paull (1998). "Proteolytic inactivation of MAP-kinase-kinase by anthrax
406 lethal factor." Science **280**(5364): 734-737.
407 Ekiert, D. C., G. Bhabha, G. L. Isom, G. Greenan, S. Ovchinnikov, I. R. Henderson, J. S. Cox and R. D. Vale
408 (2017). "Architectures of lipid transport systems for the bacterial outer membrane." Cell **169**(2): 273-
409 285. e217.
410 Emsley, P. and K. Cowtan (2004). "Coot: model-building tools for molecular graphics." Acta
411 Crystallographica Section D: Biological Crystallography **60**(12): 2126-2132.

412 Feld, G. K., K. L. Thoren, A. F. Kintzer, H. J. Sterling, Tang, II, S. G. Greenberg, E. R. Williams and B. A.
413 Krantz (2010). "Structural basis for the unfolding of anthrax lethal factor by protective antigen
414 oligomers." Nat Struct Mol Biol **17**(11): 1383-1390.
415 Fisher, M. T. and S. Naik (2019). Systems and methods for identifying protein stabilizers, Google Patents.
416 Frank, J. (2017). "Time-resolved cryo-electron microscopy: Recent progress." Journal of structural
417 biology **200**(3): 303-306.
418 Gogol, E., N. Akkaladevi, L. Szerszen, S. Mukherjee, L. Chollet-Hinton, H. Katayama, B. Pentelute, R.
419 Collier and M. Fisher (2013). "Three dimensional structure of the anthrax toxin translocon–lethal factor
420 complex by cryo-electron microscopy." Protein Science **22**(5): 586-594.
421 Gupta, P., S. Singh, A. Tiwari, R. Bhat and R. Bhatnagar (2001). "Effect of pH on stability of anthrax lethal
422 factor: correlation between denaturation and activity." Biochemical and biophysical research
423 communications **284**(3): 568-573.
424 Hardenbrook, N. J., S. Liu, K. Zhou, K. Ghosal, Z. H. Zhou and B. A. Krantz (2020). "Atomic structures of
425 anthrax toxin protective antigen channels bound to partially unfolded lethal and edema factors." Nature
426 communications **11**(1): 1-10.
427 Jas, G. S., E. W. Childs and K. Kuczera (2019). "Kinetic pathway analysis of an α-helix in two protonation
428 states: Direct observation and optimal dimensionality reduction." The Journal of chemical physics
429 **150**(7): 074902.
430 Jiang, J., B. L. Pentelute, R. J. Collier and Z. H. Zhou (2015). "Atomic structure of anthrax PA pore
431 elucidates toxin translocation." Nature **521**(7553): 545.
432 Katayama, H., J. Wang, F. Tama, L. Chollet, E. Gogol, R. Collier and M. Fisher (2010). "Three-dimensional
433 structure of the anthrax toxin pore inserted into lipid nanodiscs and lipid vesicles." Proceedings of the
434 National Academy of Sciences **107**(8): 3453-3457.
435 Kintzer, A. F., K. L. Thoren, H. J. Sterling, K. C. Dong, G. K. Feld, I. I. Tang, T. T. Zhang, E. R. Williams, J. M.
436 Berger and B. A. Krantz (2009). "The protective antigen component of anthrax toxin forms functional
437 octameric complexes." Journal of molecular biology **392**(3): 614-629.
438 Knapp, O., E. Maier, E. Waltenberger, C. Mazuet, R. Benz and M. R. Popoff (2015). "Residues involved in
439 the pore-forming activity of the C lostridium perfringens iota toxin." Cellular microbiology **17**(2): 288-
440 302.
441 Krantz, B. A., A. Finkelstein and R. J. Collier (2006). "Protein translocation through the anthrax toxin
442 transmembrane pore is driven by a proton gradient." Journal of molecular biology **355**(5): 968-979.
443 Krantz, B. A., R. A. Melnyk, S. Zhang, S. J. Juris, D. B. Lacy, Z. Wu, A. Finkelstein and R. J. Collier (2005). "A
444 phenylalanine clamp catalyzes protein translocation through the anthrax toxin pore." Science **309**(5735):
445 777-781.
446 Krantz, B. A., A. D. Trivedi, K. Cunningham, K. A. Christensen and R. J. Collier (2004). "Acid-induced
447 unfolding of the amino-terminal domains of the lethal and edema factors of anthrax toxin." Journal of
448 molecular biology **344**(3): 739-756.
449 Ma, P., A. E. Cardenas, M. I. Chaudhari, R. Elber and S. B. Rempe (2017). "The impact of protonation on
450 early translocation of anthrax lethal factor: Kinetics from molecular dynamics simulations and
451 milestoning theory." Journal of the American Chemical Society **139**(42): 14837-14840.
452 Machen, A., N. Akkaladevi, C. Trecazzi, P. O'Neil, S. Mukherjee, Y. Qi, R. Dillard, W. Im, E. Gogol and T.
453 White (2017). "Asymmetric cryo-EM structure of anthrax toxin protective antigen pore with lethal factor
454 N-terminal domain." Toxins **9**(10): 298.
455 Machen, A. J., P. T. O'Neil, B. L. Pentelute, M. T. Villar, A. Artigues and M. T. Fisher (2018). "Analyzing
456 Dynamic Protein Complexes Assembled On and Released From Biolayer Interferometry Biosensor Using
457 Mass Spectrometry and Electron Microscopy." JoVE (Journal of Visualized Experiments)(138): e57902.
458 Mastronarde, D. N. (2005). "Automated electron microscope tomography using robust prediction of
459 specimen movements." Journal of structural biology **152**(1): 36-51.

460 Miller, C. J., J. L. Elliott and R. J. Collier (1999). "Anthrax protective antigen: prepore-to-pore conversion."
461 Biochemistry **38**(32): 10432-10441.
462 Mogridge, J., K. Cunningham and R. J. Collier (2002). "Stoichiometry of anthrax toxin complexes."
463 Biochemistry **41**(3): 1079-1082.
464 Neumeyer, T., B. Schiffler, E. Maier, A. E. Lang, K. Aktories and R. Benz (2008). "Clostridium botulinum C2
465 Toxin IDENTIFICATION OF THE BINDING SITE FOR CHLOROQUINE AND RELATED COMPOUNDS AND
466 INFLUENCE OF THE BINDING SITE ON PROPERTIES OF THE C2II CHANNEL." Journal of Biological
467 Chemistry **283**(7): 3904-3914.
468 Pentelute, B. L., O. Sharma and R. J. Collier (2011). "Chemical dissection of protein translocation through
469 the anthrax toxin pore." Angewandte Chemie International Edition **50**(10): 2294-2296.
470 Pettersen, E. F., T. D. Goddard, C. C. Huang, G. S. Couch, D. M. Greenblatt, E. C. Meng and T. E. Ferrin
471 (2004). "UCSF Chimera—a visualization system for exploratory research and analysis." Journal of
472 computational chemistry **25**(13): 1605-1612.
473 Piper, S. J., L. Brillault, R. Rothnagel, T. I. Croll, J. K. Box, I. Chassagnon, S. Scherer, K. N. Goldie, S. A.
474 Jones and F. Schepers (2019). "Cryo-EM structures of the pore-forming A subunit from the Yersinia
475 entomophaga ABC toxin." Nature communications **10**(1): 1952.
476 Punjani, A., J. L. Rubinstein, D. J. Fleet and M. A. Brubaker (2017). "cryoSPARC: algorithms for rapid
477 unsupervised cryo-EM structure determination." Nature Methods **14**(3): 290-296.
478 Ritchie, T., Y. Grinkova, T. Bayburt, I. Denisov, J. Zolnerciks, W. Atkins and S. Sligar (2009). "Chapter
479 eleven-reconstitution of membrane proteins in phospholipid bilayer nanodiscs." Methods in enzymology
480 **464**: 211-231.
481 Santelli, E., L. A. Bankston, S. H. Leppia and R. C. Liddington (2004). "Crystal structure of a complex
482 between anthrax toxin and its host cell receptor." Nature **430**(7002): 905.
483 Sugawara, T., D. Yamashita, K. Kato, Z. Peng, J. Ueda, J. Kaneko, Y. Kamio, Y. Tanaka and M. Yao (2015).
484 "Structural basis for pore-forming mechanism of staphylococcal α-hemolysin." Toxicon **108**: 226-231.
485 Thoren, K. L. and B. A. Krantz (2011). "The unfolding story of anthrax toxin translocation." Molecular
486 microbiology **80**(3): 588-595.
487 Wigelsworth, D. J., B. A. Krantz, K. A. Christensen, D. B. Lacy, S. J. Juris and R. J. Collier (2004). "Binding
488 stoichiometry and kinetics of the interaction of a human anthrax toxin receptor, CMG2, with protective
489 antigen." Journal of Biological Chemistry **279**(22): 23349-23356.
490 Wilson, D. N. and R. Beckmann (2011). "The ribosomal tunnel as a functional environment for nascent
491 polypeptide folding and translational stalling." Current opinion in structural biology **21**(2): 274-282.
492 Young, J. A. and R. J. Collier (2007). "Anthrax toxin: receptor binding, internalization, pore formation,
493 and translocation." Annu. Rev. Biochem. **76**: 243-265.
494 Zhang, F., M. Hu, G. Tian, P. Zhang, D. Finley, P. D. Jeffrey and Y. Shi (2009). "Structural insights into the
495 regulatory particle of the proteasome from Methanocaldococcus jannaschii." Molecular cell **34**(4): 473-
496 484.
497 Zhang, S., A. Finkelstein and R. J. Collier (2004). "Evidence that translocation of anthrax toxin's lethal
498 factor is initiated by entry of its N terminus into the protective antigen channel." Proceedings of the
499 National Academy of Sciences **101**(48): 16756-16761.

500
501

502

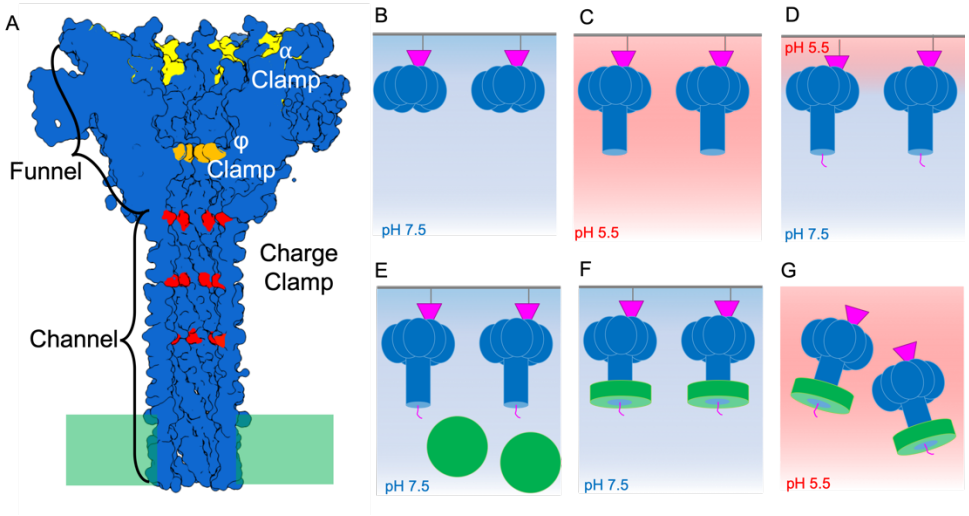

503

504 **Figure 1. Anthrax toxin immobilization, translocation, and nanodisc stabilization (TITaNS)**

505 **method** (A) PA (blue) pore lumen side view slice showing funnel shape from α clamp (yellow)

506 to Φ clamp (orange) with charge clamp (red) inside pore β barrel. (B) Immobilization of LF_N

507 (magenta) and $PA_{prepore}$ (blue) on thiol sepharose beads (grey surface) to prevent aggregation. (C)

508 $PA_{prepore}$ transition to PA_{pore} under acidic conditions (D) LF_N translocation through PA_{pore}

509 initiated through diffuse pH gradient. (E) Addition of pre-nanodisc micelle (green). (F) Detergent

510 dialyzed to form lipid bilayer nanodisc. (G) LF_N-PA_{pore}-Nanodisc complexes released at pH 5.5

511 on cryoEM grid.

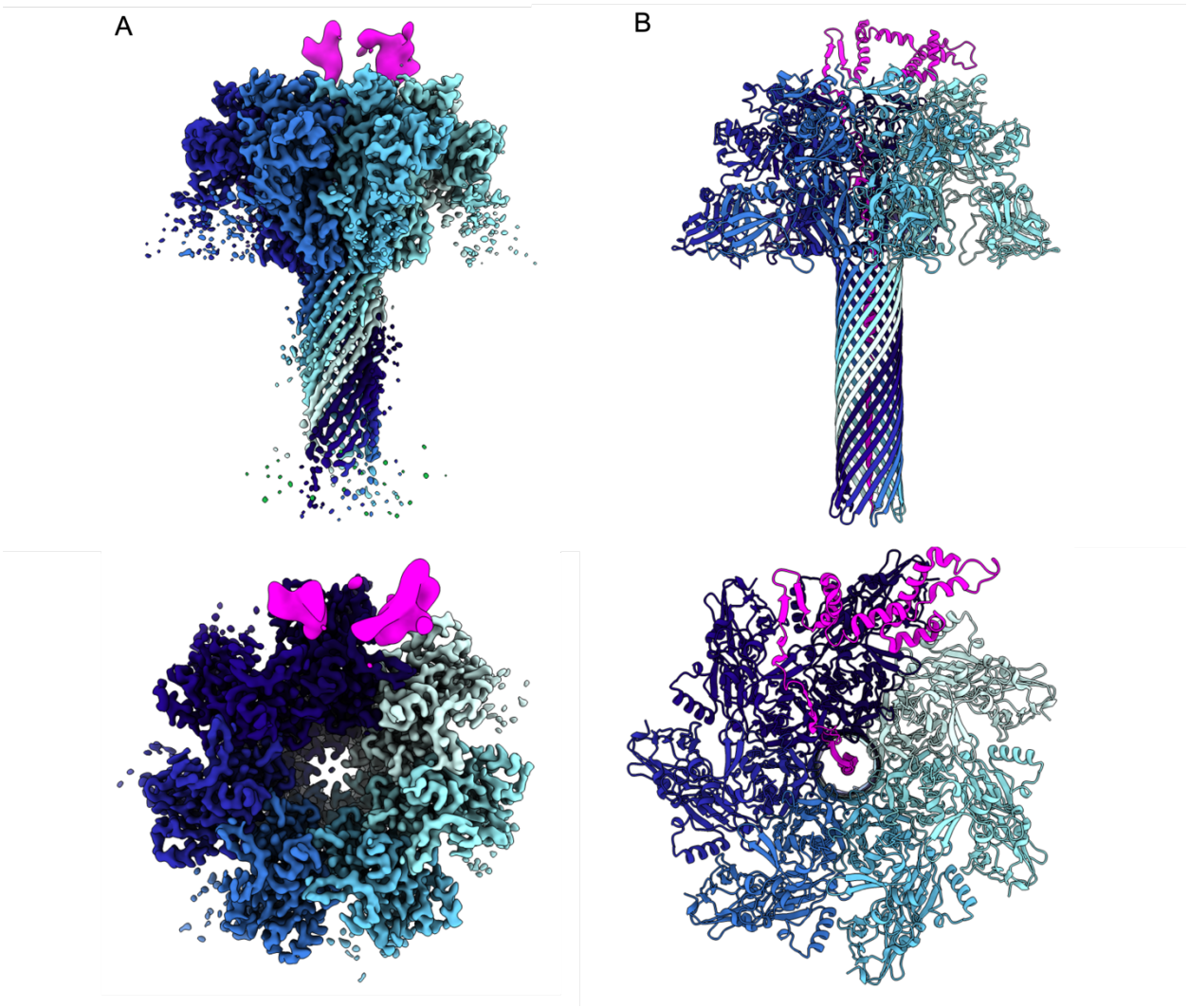

512

513

514 **Figure 2.**

515 **Overview of the anthrax complex with the N-terminal domain of lethal factor (magenta)**

516 **translocating through the protective antigen pore (blue gradient).** (A) 3.06 Å cryoEM density

517 map of LF_N and PA_{pore} with side view (top) and top down view (bottom). (B) Molecular model of

518 PA_{pore} with side view (top) and top down view (bottom).

519

520

521

522

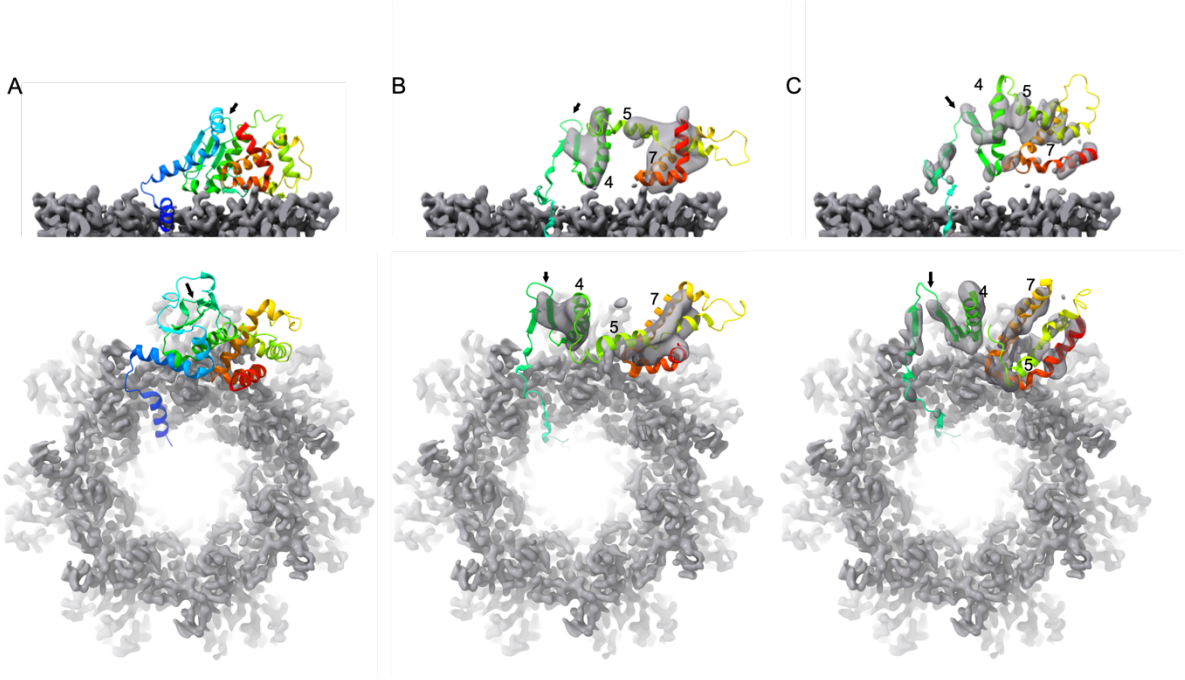

523

524

525 **Figure 3. Unfolding intermediates of translocating LF_N.** (A) Folded LF_N (6PSN) (rainbow
526 model) docked on PA_{pore} (grey map) for comparison. (B) Unfolded LF_N 1 shows separation of
527 Lobe 1 and Lobe 2 via helix 4 (green) and 7 (orange) with helix 5 (green-yellow) stretched between
528 the 2 lobes. (C) Unfolded intermediate 2 showing further unfolding, vertical separation from PA,
529 and β hairpin separation. Black arrow indicates immobilized residue E126C.

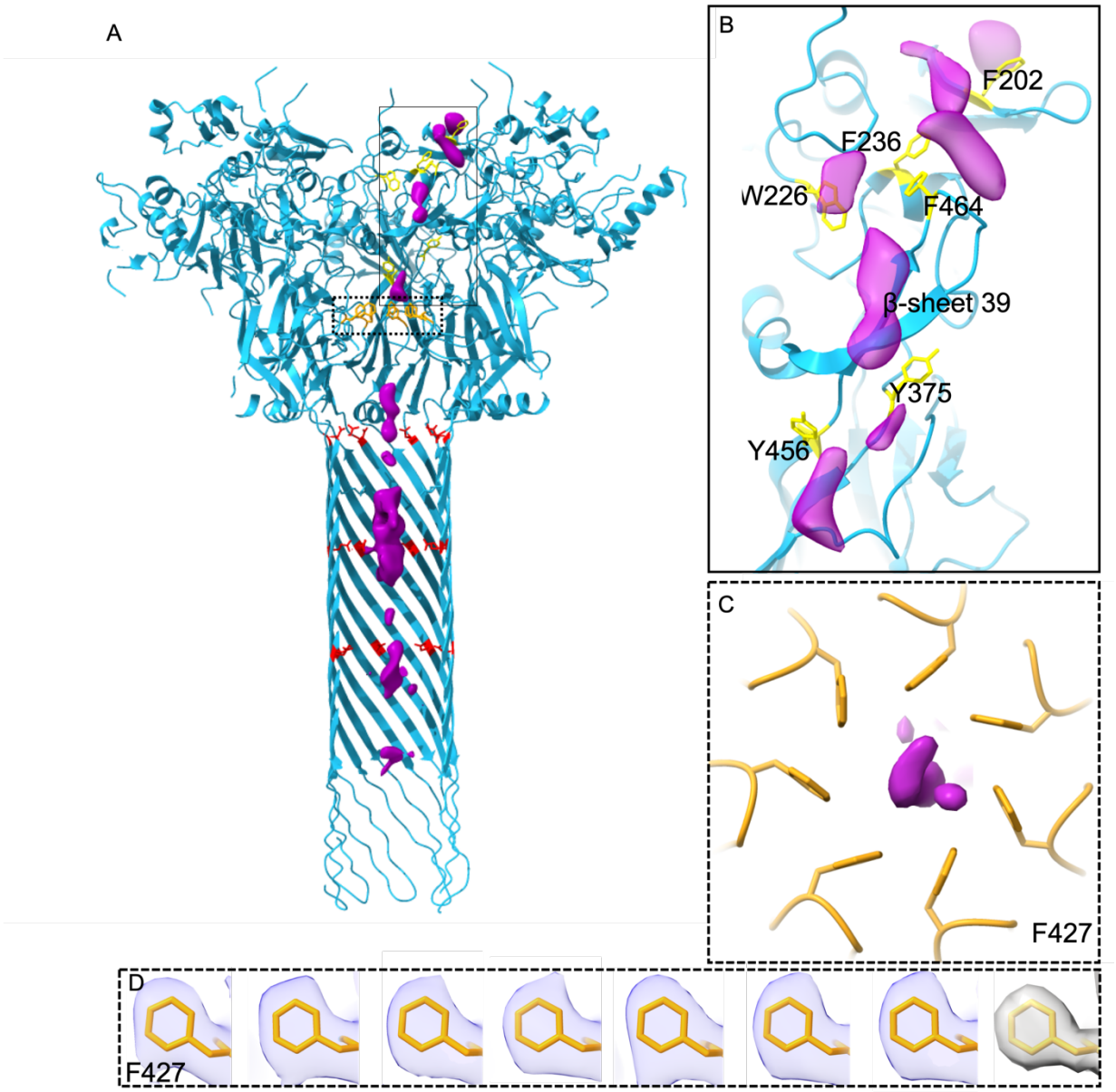

530

531 **Figure 4. Translocating LF_N visible at key clamp sites.** (A) Overview of the anthrax pore (cyan)

532 with density of tranlsocaitng LF_N (magenta). (B) close up of key hydrophobic residues (yellow) in

533 early translocation from α clamp to φ clamp.(C) Top view of Φ clamp (orange) with LF_N density

534 passing through (D) Individual F427 residues (orange) with associated cryoEM density for each

535 subunit compared to modelled density (grey, 3 Å).

536

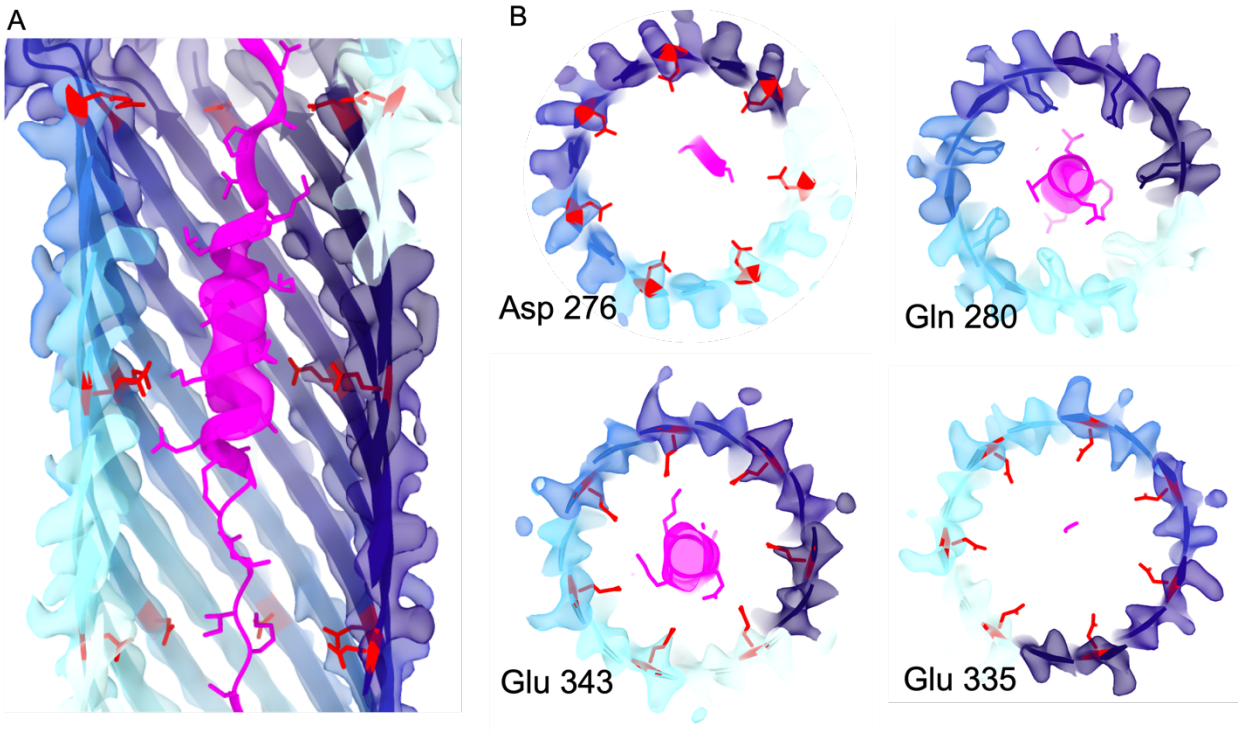

537

538 **Figure 5. Focused refinement of β barrel interior reveals refolding of LF_N** (A) Side slice of

539 PA_{pore} (blue) charge clamp (red) with LF_N density (pink) (B) Top view slices of the PA_{pore} charge

540 clamp at key acidic residues.

541

542

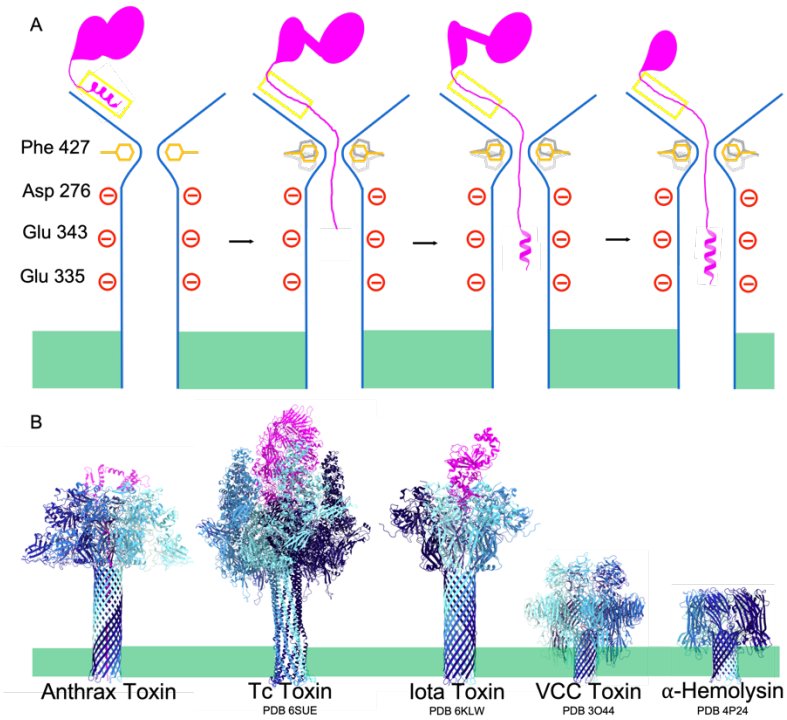

543

544 **Figure 6. Proposed AB toxin translocation mechanism.** (A) Unfolding-refolding translocation
545 model of anthrax toxin. LF_N (magenta) bound to PA_{pore} (blue) with helix bound to α clamp
546 (yellow). Under acidic conditions of the endosome, LF_N lobes separate and shift toward α clamp
547 during translocation. Unfolded peptide passes the dynamic Φ clamp (orange and grey) and acidic
548 residues are deprotonated by three PA charge clamp residues (red) in the channel. Helical portions
549 of LF_N begin to refold in the channel, disfavoring retrograde transfer, overcoming local energy
550 barriers, and ensuring proper teritiary folding. (B) Comparison of toxin pore length for toxins that
551 translocate proteins (anthrax, Tc, iota) vs toxins that disrupt ion gradients (VCC and α-Hemolysin).
552 Membrane bilayer represented in green. Note only the N-terminal domain of anthrax toxin lethal
553 factor is shown.